A reduced-geometry independent particle model calculation of high harmonic generation from closed-shell diatomic molecules

Mitsuko Murakami, Tom Kirchner, and Marko Horbatsch

Abstract: We propose a simple model to calculate high harmonic spectra from closed-shell diatomic molecules based on the time-dependent Schrödinger equation. Quasi-Coulomb potentials are used to represent the two-center geometry of a diatomic molecule in two dimensions. A few outer occupied molecular orbitals are evolved independently using a single-electron Hamiltonian, and the harmonic spectra are evaluated from a coherent sum of single-electron dipole accelerations. According to this independent particle model, harmonic spectra from individual orbitals follow the semiclassical cutoff law, but their relative strengths vary depending on molecular orientations. When the contributions from different orbitals are of comparable strength, their net spectrum extends to the inner-orbital cutoffs, and in some cases acquires a local minimum where harmonic spectra from different molecular orbitals interfere destructively because of their phase difference.

PACS Nos: 33.20.Xx, 32.80.Rm, 42.65.Ky

Résumé : Nous proposons un modèle simple pour calculer, à partir de l'équation de Schrödinger dépendante du temps, les spectres hautement harmoniques de molécules diatomiques à couches fermées. Nous utilisons des potentiels quasi-coulombiens pour représenter la géométrie à deux centres d'une molécule diatomique en deux dimensions. Un Hamiltonien à un électron permet d'évaluer l'évolution indépendante de quelques orbitales extérieures occupées et nous calculons les spectres harmoniques à partir d'une somme cohérente d'accélérations dipolaires de simples électrons. Selon ce modèle à électrons indépendants, les spectres harmoniques à partir d'orbitales à une particule suivent la loi de coupure semi-classique, mais leurs forces relatives varient suivant les orientations moléculaires. Lorsque les contributions de différentes orbitales sont de force comparable, leur spectre net s'étend aux coupures des orbitales intérieures et, dans certains cas, acquière un minimum local là où les spectres harmoniques de différentes orbitales moléculaires interfèrent de façon destructive à cause de leur différence de phase.

[Traduit par la Rédaction]

1. Introduction

Advances in molecular high harmonic generation (HHG) in the last several years have raised some questions, such as the geometric interference [1] and the orbital–orbital interference [2, 3] effects, which are not present in atomic HHG. There are two different, equally successful, approaches in atomic HHG theories; one uses the numerical solution of the time-dependent Schrödinger equation (TDSE) [4, 5], and the other uses the path-integral method known as the strong field approximation (SFA) [6, 7]. Extended SFA theories for molecular HHG that include geometric and multielectron effects have emerged in recent years. Le et al. developed a quantitative rescattering theory [8], which takes the orientation dependence of molecular ionization into account in the evaluation of the SFA propagation amplitude. Santra and Gordon used many-body perturbation theory to derive corrections to the SFA recombination amplitude [9]. Smirnova et al. incorporated self-consistent field (SCF) calculations for the bound-state orbitals into the three-step SFA theory of ref. 10, to include the effect of ionic-state transitions during HHG [11]. Most of these molecular HHG theories, however, avoid direct solution of the TDSE, because it is computationally demanding to model HHG from molecules based on the TDSE. The problem is fully three dimensional (3D) even for the simplest diatomic molecule H_2^+ [12], when the bonding axis of the molecule is not aligned with the field polarization. In addition, one must solve for the multielectron TDSE to account for the orbital–orbital interference in molecular harmonic spectra; this is in contrast to atomic HHG where the single-active-electron approximation proved adequate to explain the experimental spectra from multielectron noble gas atoms.

A computationally tractable alternative to the multielectron TDSE is time-dependent density functional theory (TDDFT). Attempts to calculate high harmonics from molecules using TDDFT have been made for H_2 [13, 14], N_2 [15, 16], F_2 [17], CO_2 [18, 19], CO [16], etc. Recently, Abu-samha and Madsen [20] solved the 3D TDSE for multielectron molecules in a TDDFT framework, and demonstrated that the mo-

Received 24 January 2012. Accepted 12 April 2012. Published at www.nrcresearchpress.com/cjp on 28 May 2012.

M. Murakami, T. Kirchner, and M. Horbatsch. Department of Physics and Astronomy, York University, Toronto, ON M3J 1P3, Canada.

Corresponding author: Mitsuko Murakami (e-mail: mitsukok@yorku.ca).

lecular tunneling theory commonly used in the SFA formulation of molecular HHG has shortcomings in predicting the peak-ionization angles for CO_2. Their findings show that the TDSE-based theories can complement the SFA approach for molecular HHG. However, the spatial grids required in 3D calculations are often too limiting to calculate HHG spectra with full details.

To understand a complicated system, it is useful to isolate each component and observe its influence on the results. For molecular HHG, that includes: (*i*) electronic structure, (*ii*) multicenter geometry and rovibrational degrees of freedom, (*iii*) multielectron ionization, and (*iv*) macroscopic propagation effects. One frequently employed model for such studies in strong-field physics is a reduced-dimensional atom or molecule based on quasi-Coulomb potentials [21]. In this model, essential characteristics of strong-field interactions can be addressed separately, for example, the elliptic polarization effect [22, 23], two-center geometry [24], nuclear motion [25, 26], and electron–electron correlation [13, 27–29]. The reduced dimensionality allows to carry out numerical calculations with high accuracy.

In this paper, we study the effect of orbital–orbital interference in molecular HHG using two-dimensional (2D) quasi-Coulomb potentials. The TDSE is solved for a few outer occupied molecular orbitals (MOs) in the limit of an independent particle model (IPM), that is, each MO is evolved independently under a single-electron Hamiltonian. The effect of electron–electron screening is represented by a model potential, but exchange (and correlation) effects are neglected. It is interesting to observe whether such a simple IPM calculation does, in fact, produce orbital–orbital interference structures. The harmonic spectrum is evaluated in two different ways, that is, either from a coherent sum of individual MO spectra, or from the net dipole acceleration as it arises in the framework of TDDFT. These two different prescriptions do not yield identical spectra because we use an approximate single-electron potential.

We focus on modeling HHG from closed-shell diatomic molecules, whose ground state energies are adjusted for the outermost occupied MOs of N_2 and F_2. The resulting spectra are examined by using the recently measured molecular spectra by Wörner et al. [30] as references. Given that the theoretical supporting argument in ref. 30 used a SFA approach [10, 11] without macroscopic propagation effects [31], we consider it meaningful to verify their findings against the single-molecule calculation according to the TDSE. The present work is accomplishing this task in a reduced geometry.

The outline of the paper is as follows. In Sect. 2, we introduce the model, and describe the numerical methods for the TDSE and the initial value problem. Section 3 comprises our results; the ground-state MOs of the N_2- and F_2-like 2D model molecules are presented in Sect. 3.1; the connection between ionization probabilities and harmonic yield for these two model molecules is discussed in Sect. 3.2, and their harmonic spectra are examined in Sect. 3.3. The phase difference among the individual MO spectra from the F_2-like 2D molecule are investigated in Sect. 3.4 for some evidence of the orbital–orbital interference. Section 4 summarizes the results. Atomic units ($\hbar = m_e = e = 1$) will be used throughout, unless stated otherwise.

2. Methods

2.1. Model

Let (x_1, y_1) and (x_2, y_2) be the coordinates of the two nuclei in a diatomic molecule, such that

$$x_i = \pm\frac{R}{2}\cos\theta \qquad y_i = \pm\frac{R}{2}\sin\theta \qquad i = 1, 2 \tag{1}$$

where R is the internuclear distance, and θ is the angle between the molecular axis and the driving-laser polarization. For simplicity, the nuclear motion is neglected. The interaction of a diatomic molecule and a laser field $E(t)$ polarized along the x-axis is modeled by the following set of 2D single-electron TDSEs

$$i\frac{\partial}{\partial t}\psi_n(x, y, t) = H\psi_n(x, y, t) \tag{2}$$

Here $n = 1, 2, \ldots, N$ runs through the number of active MOs. The model Hamiltonian in length gauge is given by

$$H = \frac{-1}{2}\left(\frac{\partial^2}{\partial x^2} + \frac{\partial^2}{\partial y^2}\right) + U(x, y) + v_{ee}(x, y) + xE(t) \tag{3}$$

where $E(t) = E_o(t)\sin\omega_o t$ for a given pulse-envelope function $E_o(t)$, and

$$U(x, y) = \sum_{i=1,2}\frac{-Z_i}{\sqrt{(x - x_i)^2 + (y - y_i)^2 + \epsilon}} \tag{4}$$

$$v_{ee}(x, y) = \frac{-1 + Z_1 + Z_2}{\sqrt{x^2 + y^2 + \mu}} \tag{5}$$

Here, Z_i ($i = 1, 2$), ϵ, and μ are constants determined as follows. For N_2 (F_2), the first four (five) eigenfunctions corresponding to the lowest energies are chosen to represent occupied MOs, so that the highest-occupied molecular orbital (HOMO) has the same symmetry as real N_2 (F_2) when projected on a plane. Given the spin degeneracy, the effective charge numbers are therefore set to be $Z_1 = Z_2 = 4$ for N_2 and $Z_1 = Z_2 = 5$ for F_2. The innermost electrons corresponding to the $1\sigma_g$ and $1\sigma_u$ states are assumed frozen. The nuclear screening parameter ϵ in (4) is set to 0.5, a typical value for 2D calculations [1], while the electron–electron screening parameter μ in (5) is adjusted to produce the correct energy for the HOMO of N_2 or F_2. This prescription for the model parameters naturally leads to the correct HOMO-1 energy as well (cf. Table 1 in Sect. 3). For all results shown in this paper, the pulse-envelope function $E_o(t)$ has a $\cos^2$ shape centered around $t = 0$ with a total duration of 20 cycles including rise and fall.

Potential (5) models a static electron–electron screening effect. The exact TDDFT potential would have to include the time-dependent Hartree potential and the exchange–correlation potential. Neither of them is represented by model potential (5). Note that a time-depenedent mean-field potential would lead to the problem of nonexponential decay in a monochromatic laser field [32]. The overall potential in model Hamiltonian (3) has the correct asymptotic behavior for single electron removal. Because all the MOs are propagated in the same potential, their orthogonality is preserved at all times.

2.2. Integration scheme

The time-evolution operator is split as

$$e^{-iH\delta t/2} \simeq e^{-iV\delta t/2} e^{-iT\delta t} e^{-iV\delta t/2} \tag{6}$$

where

$$V = U(x, y) + v_{ee}(x, y) + xE(t) \tag{7}$$

$$T = \frac{-1}{2}\left(\frac{\partial^2}{\partial x^2} + \frac{\partial^2}{\partial y^2}\right) = \frac{p_1^2}{2} + \frac{p_2^2}{2} \tag{8}$$

The propagator for the kinetic energy operator T is applied in momentum space using fast Fourier transforms. Equation (2) is solved on a 2D cartesian spatial grid whose x-axis is aligned with the laser polarization, and extends either to ±5 times the classical oscillator radius $\alpha_o = E_o(0)/\omega_o^2$ or to ±140 au, whichever is larger, whereas the y-axis range is kept at a quarter of this size. The parts of the wave function that reach the spatial boundaries are absorbed by a gobbler function to avoid wraparound flow [33]. The results in this paper are obtained using resolutions of $\Delta x = \Delta y = 0.2$ and $\Delta t = 0.05$.

2.3. Initial states

To find the initial MOs, we solve the eigenvalue problem

$$H_o u_n(x, y) = \varepsilon_n u_n(x, y) \tag{9}$$

for $n = 1, 2, \ldots, N$, where

$$H_o = \frac{-1}{2}\left(\frac{\partial^2}{\partial x^2} + \frac{\partial^2}{\partial y^2}\right) + U(x, y) + v_{ee}(x, y) \tag{10}$$

Eigenvector–eigenvalue pairs are obtained by propagating an orthogonal set of initial wave functions in negative imaginary time $\tau = -it$. This is equivalent to evolving a set of diffusion equations, given by

$$-\frac{\partial}{\partial t} f_n(x, y, t) = H_o f_n(x, y, t) \tag{11}$$

for sufficiently long time (i.e., $f_n(x, y, t \to \infty) = u_n(x, y)$). Equations (11) are solved using the same spatial grid and numerical scheme used for the TDSE (Sect. 2.2) but with a temporal resolution of $\Delta t = 0.01$, while imposing the orthonormality condition among the f_n at each time step.

2.4. Harmonic spectra

From the solutions of (2), the dipole acceleration is found by using Ehrenfest's theorem. Two alternative calculations are possible for the *net* dipole acceleration of a molecule. The more intuitive approach is the following:

IPM perspective: for each of the N active MOs, we calculate the dipole acceleration along the laser polarization axis as

$$a_n(t) = \langle \psi_n(t) | \nabla V \cdot \hat{\boldsymbol{e}}_x | \psi_n(t) \rangle \tag{12}$$

where V is given by (7). The net dipole acceleration is found as their coherent sum, that is,

$$a^V(t) = \sum_{n=1}^{N} g_n a_n(t) \tag{13}$$

where g_n is the occupation number for the nth active MO.

Equation (12) is used to calculate the *individual* harmonic spectrum of each MO.

If a Kohn–Sham type calculation with the exact exchange–correlation potential were used (i.e., if the orbital densities obtained from (2) would sum up to the exact one-particle density of the many-electron system) then the zero-force theorem [34, 35] of TDDFT would apply and v_{ee} in (3) would not contribute to the dipole acceleration. Accordingly, we also consider the following alternative.

TDDFT perspective: the net dipole acceleration along the laser polarization axis is given by

$$a^W(t) = \sum_{n=1}^{N} g_n \langle \psi_n(t) | \nabla W \cdot \hat{\boldsymbol{e}}_x | \psi_n(t) \rangle \tag{14}$$

where

$$W = U(x, y) + xE(t) \tag{15}$$

Note that, as v_{ee} in our model given by (5) is approximate, net dipole accelerations (13) and (14) are different, and it is not clear a priori which one is to be preferred [36]. One of the aims of the present work is to provide a comparison of both prescriptions. The TDDFT perspective does not allow an evaluation of the individual harmonic spectrum.

The occupation number g_n for each active MO is determined as follows. The N_2 molecule has 14 electrons in total, four of which are frozen in the $1\sigma_g$ and $1\sigma_u$ states (Sect. 2.1). In SCF Hartree–Fock (HF) calculations in 3D, the 10 remaining electrons are distributed over four MOs as [37] $(2\sigma_g)^2(2\sigma_u)^2(1\pi_u)^4(3\sigma_g)^2$. The π_u orbital is degenerate because of its ±1 magnetic quantum numbers. In our 2D model, the analogous orbitals o1–o4 are found, and are assumed to accommodate electrons in a similar manner as $(o1)^2(o2)^2(o3)^4(o4)^2$.

Similarly, the SCF–HF configuration for 14 electrons in the five outermost occupied MOs of the F_2 molecule is [38] $(2\sigma_g)^2(2\sigma_u)^2(3\sigma_g)^2(1\pi_u)^4(1\pi_g)^4$ and therefore we assume their configuration in 2D according to $(o1)^2(o2)^2(o3)^2(o4)^4(o5)^4$. Model hamiltonian (3) does not depend on the occupation numbers, as the IPM we adopt does not involve a SCF calculation.

In the analysis below, the individual MO spectrum in Sect. 3.3.1 is found as $|\tilde{a}_n(\omega)|^2$, where $\tilde{a}_n(\omega)$ is the Fourier transform of (12). The net dipole spectrum $D(\omega)$ in Sect. 3.3.2 on the other hand, is evaluated in two ways, either from (13) as $|\tilde{a}^V(\omega)|^2$ or from (14) as $|\tilde{a}^W(\omega)|^2$. In practice, only a few valence MOs (i.e., the HOMO ($n = N$), the HOMO-1 ($n = N - 1$), and the HOMO-2 ($n = N - 2$)) are necessary for the convergence of $D(\omega)$ in both cases. All the dipole accelerations (i.e., (12), (13), and (14)) are multiplied by a Welch window before the Fourier transform to obtain clean spectra. Because of the absorbing boundaries (Sect. 2.2), the norm of the wave function used to evaluate the dipole acceleration becomes less than one during the time evolution of the TDSE.

Fig. 1. The six lowest-energy MOs of the 2D N_2 molecule. The molecular axis is in the horizontal direction. Contour lines are drawn in intervals of ±0.1.

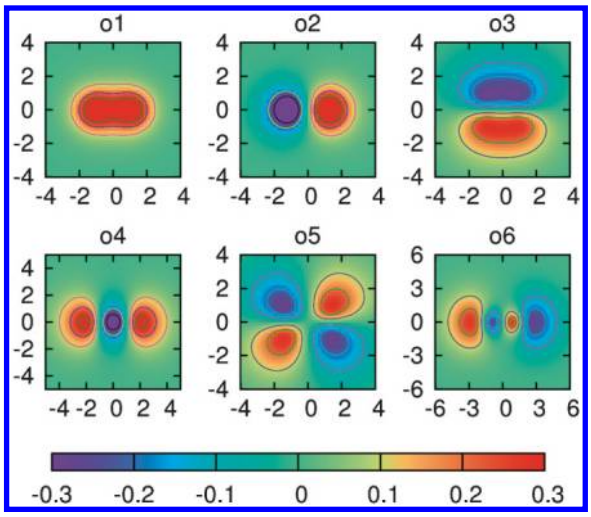

Table 1. Absolute values of the six lowest stationary-state MO energies of the model molecules (2D) and the corresponding experimental ionization energies (Exp.) in eV.

N_2				F_2			
2D		Exp. [39]		2D		Exp. [43]	
o6	8.6	—	—	o6	14.7	—	—
o5	9.2	—	—	o5*	15.7	$1\pi_g$	15.7
o4*	15.2	$3\sigma_g$	15.5	o4	19.0	$1\pi_u$	18.98
o3	16.9	$1\pi_u$	16.8	o3	19.7	$3\sigma_g$	21.0
o2	40.7	$2\sigma_u$	18.6	o2	55.6	—	—
o1	49.7	$2\sigma_g$	37.3	o1	57.7	—	—

*HOMO

3. Results

3.1. Ground states of 2D model molecules

3.1.1. N_2-like molecule

To model the N_2 molecule in 2D, we let the internuclear distance be $R = 2.1$ (to reflect the experimentally measured equilibrium distance $R = 2.068$ [39]) and use the effective charge numbers $Z_1 = Z_2 = 4$, to obtain four orthogonal MOs that have symmetries analogous to the first four valence MOs of the real N_2 molecule predicted by SCF–HF calculations [37]. Figure 1 shows the six lowest-energy MOs of the 2D N_2 molecule obtained with $\mu = 2.5$. The energies and the corresponding experimental values are summarized in Table 1. We find that our 2D model produces correct energies for the first two valence MOs of N_2. However, the ionization energies of the innermost MOs (o1 and o2) in the 2D model are too large in comparison with the experimental values. This limits our analysis in that the harmonic contribution from the HOMO-2 orbital of N_2 must be disregarded, although its experimentally measured ionization energy suggests that a sizeable contribution from this orbital is indeed possible.

3.1.2. F_2-like molecule

By increasing the effective charge numbers in the Hamiltonian to $Z_1 = Z_2 = 5$, we can investigate the case when the HOMO is the antibonding π state (which has four lobes with alternating signs), as is the case for the O_2 and F_2 molecules. We will consider only the F_2 molecule because the O_2 molecule has additional complications associated with its open-shell structure [40–42]. Choosing the parameters $\mu = 2.6$ and $R = 2.7$ (experimental value: $R = 2.712$ [43]) yields the correct HOMO energy of F_2 for the o5 state. As Table 1 shows, the stationary-state energies of the first three valence MOs of the 2D F_2 molecule are in good agreement with the experimental values. The six lowest-energy MOs of F_2 are found in Fig. 2. Notice that, as compared to the N_2 molecule in Fig. 1, the symmetries of the o3 and o4 states (viz., bonding π state or σ state) are reversed in Fig. 2. This behavior is consistent with SCF–HF calculations [37, 38].

Fig. 2. Same as Fig. 1, but for the 2D F_2 molecule.

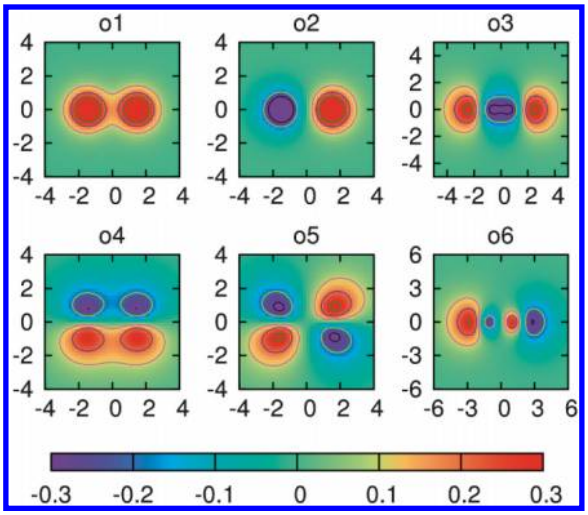

3.2. Ionization probabilities

As mentioned in Sect. 2, the norm of the wave functions becomes less than one during the time evolution of (2) because of the absorbing boundaries. These absorbed parts of the wave functions can physically be interpreted as ionizing to infinity, that is, we can infer the (permanent) ionization probabilities of the MOs from the norm of the wave functions [19, 40, 41].

Figure 3 shows the norm of a few valence-MO wave functions of the 2D N_2 and F_2 molecules as a function of time while driven by an 800 nm laser field of peak-intensity 2×10^{14} W cm^{-2}. Our model calculation predicts that the HOMO of F_2 (o5), which has antibonding character, ionizes less than the HOMO of N_2 (o4) when $\theta = 0$ and $\pi/2$, despite their similar binding energies (cf. Table 1). This is consistent with the prediction in ref. 44, that the ionization from antibonding MOs is suppressed when their nodal plane is parallel to the driving laser field.

When comparing the orientational dependence for the bonding σ orbitals (o4 in N_2 and o3 in F_2) in Fig. 3, we notice a common trend: ionization is favored when the molecular axis is aligned with the laser field ($\theta = 0$), and suppressed when $\theta = \pi/2$. The situation is not as obvious in the case of the bonding π orbitals (o3 in N_2 and o4 in F_2): the ionization of the o3 state in N_2 is strongly suppressed when $\theta = 0$, while the o4 state in F_2 is ionized preferentially for small θ.

Fig. 3. Norm of valence MOs during the HHG driven by an 800 nm, 2×10^{14} W cm^{-2} peak-intensity laser field as a function of time given in laser cycles.

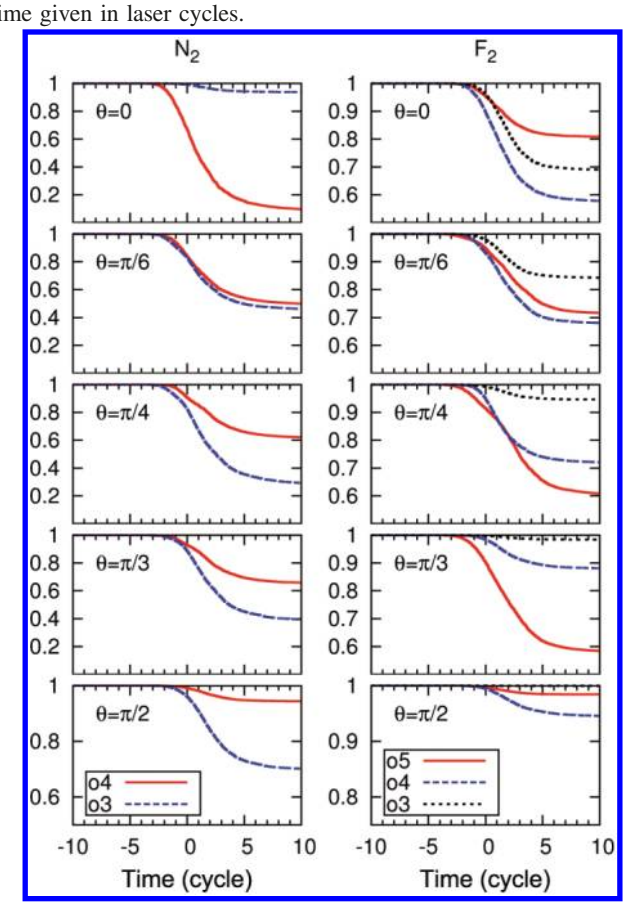

The wave-function contours of the o3 state in Fig. 1 and the o4 state in Fig. 2 show that these orbitals of equal MO symmetry do have qualitative differences, that is, the electron density within a π-lobe is somewhat separated in F_2 but not in N_2, which could cause electrons in F_2 to ionize along the molecular axis more easily than in the perpendicular direction. As illustrated by this example, the orientational dependence of molecular ionization in a strong laser field implied from Fig. 3 seems far from trivial. The conclusion drawn in ref. 19, for the case of CO_2, that the MOs ionize most when they have maximum density along the laser axis, perhaps should not be generalized to all linear molecules.

The 2D model utilizing a quasi-Coulomb potential ionizes more easily than the real 3D case, and thus the ionization probabilities of the 2D model molecules are expected to be comparable with experimental data using higher driving-laser intensities. Nevertheless, as the scope of this paper is to calculate the harmonic spectra in accordance with what is measured in ref. 30, the same driving-laser intensities as used in the experiment ($1–2 \times 10^{14}$ W cm^{-2}) are chosen to generate high harmonics.

3.3. Harmonic spectra from 2D diatomic molecules

3.3.1. Individual MO spectra

In this section, we present individual MO spectra (i.e., the squared modulus of the Fourier transform of (12)). The frequency and the peak intensity of a driving laser field are the same as in the ionization analysis of Sect. 3.2 (i.e., 800 nm and 2×10^{14} W cm^{-2}). For both N_2 and F_2 molecules modeled in this work, the lowest two MOs (o1 and o2) are neglected in the following analysis because their harmonic contributions are negligibly small due to the large ionization energies (cf. Table 1).

Fig. 4. Individual harmonic spectra $|\tilde{a}_n(\omega)|^2$ (in arbitrary units) from valence MOs of the 2D N_2 molecule driven by an 800 nm, 2×10^{14} W cm^{-2} peak-intensity laser field. Vertical lines indicate the positions of semiclassical cutoffs.

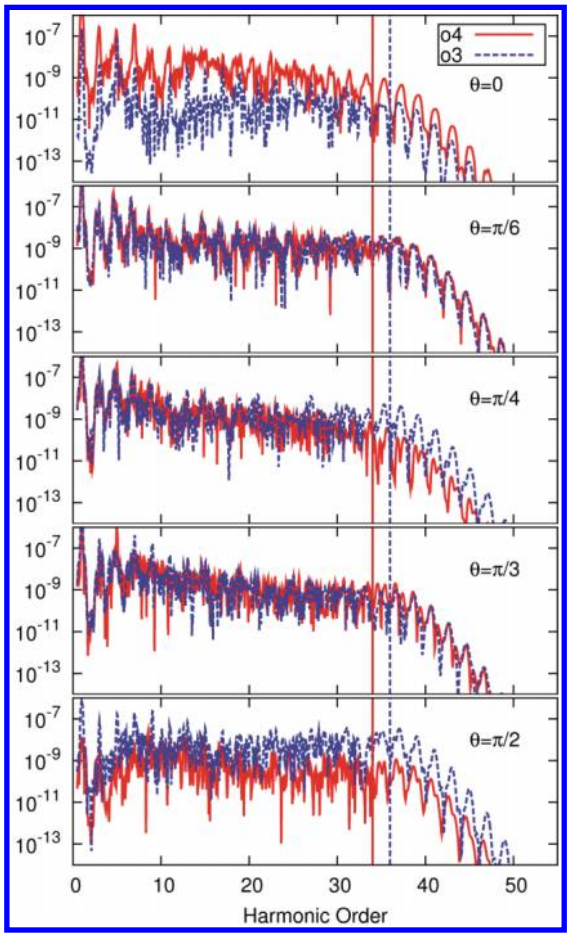

Figure 4 shows the high harmonic spectra from the first two valence MOs of the 2D N_2 molecule. Our IPM calculation predicts that each MO spectrum strictly follows the semiclassical cutoff law of ref. 45, regardless of molecular orientation and electronic structure (i.e., their intensities always fall off at the cutoff frequencies given by $I_p + 3.17U_p$, where I_p is the ionization potential of the MO considered, and U_p is the ponderomotive energy of the driving laser field). This finding that the cutoff law holds true for molecular HHG may appear to be in conflict with the previous experiment by Shan et al. [46] in which harmonic spectra of O_2 were shown to extend beyond those of Xe despite their similar ionization energies. However, the harmonics in ref. 46, were generated at saturation intensities, which were different for O_2 and Xe. In Sect. 3.3.2, we find that the position of the cutoff in our 2D N_2 spectra is in agreement with the experiment in ref. 30, using moderate driving laser intensities.

Fig. 5. Same as Fig. 4 but for the 2D F_2 molecule.

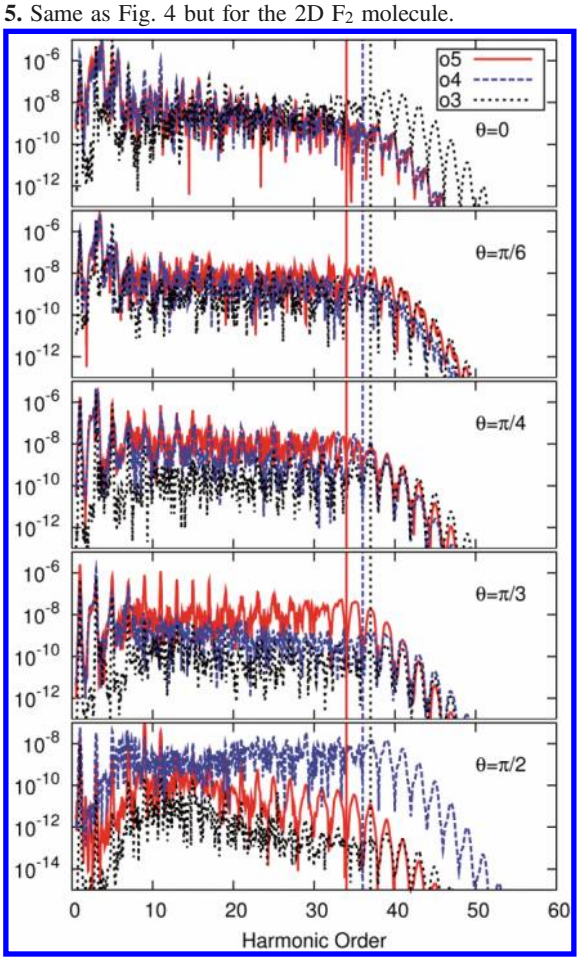

Another important observation in Fig. 4 is that the overall intensity of the individual MO spectra weakens when the molecular orientation causes ionization suppression, which can be inferred from the less diminishing norm in Fig. 3 (i.e., $\theta = 0$ for o3 and $\theta = \pi/2$ for o4). This makes sense from the point of view that less ionization means fewer electrons are available to participate in HHG.

The same general trend as known for atomic high harmonic spectra is found in Fig. 4 (i.e., each MO spectrum exhibits a plateau region with uniform intensity followed by an abrupt falloff [4, 5, 47]). The harmonics in the plateau do not have clear peaks because of the interference between the well-known short and long trajectories, according to the SFA description of HHG [7]. This degeneracy is not observed in experiments because the propagation through the atomic–molecular gas jet selects only the short electron path and locks the plateau harmonics in phase [48]. Beyond the semiclassical cutoff frequency, the short-path solution and the long-path solution merge into one. As a result, the spectra in Fig. 4 beyond the cutoff exhibit well-resolved harmonics appearing only at odd orders due to the inversion symmetry of the system along the driving laser field.

In Fig. 5, harmonic spectra from the first three valence MOs of the 2D F_2 molecule are shown. Here, in addition to the remarks made for the N_2 spectra, we observe the following. The harmonic intensity from the HOMO (o5) of F_2 weakens when $\theta = 0$ and $\pi/2$ because of the ionization suppression described in Sect. 3.2. As a result, the harmonic spectra from the inner MOs become competitive in strength at these molecular orientations. The HOMO-1 (o4) dominates when $\theta = \pi/2$, which is understandable, as it is ionizing most among the three valence MOs at this orientation in Fig. 3. On the other hand, the HOMO-2 (o3) dominates when $\theta = 0$ although its final ionization probability in Fig. 3 is smaller than that of the HOMO-1. Looking at the ionization profiles of these two MOs in Fig. 3 more closely, however, one notices that the HOMO-2 survives through the peak of the driving laser ($t = 0$) better than the HOMO-1 does. This should enhance the harmonic intensities particularly in the cutoff region, as is confirmed in Fig. 5.

Moreover, the o5 spectrum for $\theta = \pi/2$ exhibits an unusual behavior, namely, the spectral peaks are well-resolved at all odd harmonic orders even in the plateau region. The sharp peaks below the 20th harmonic indicate that they originate from short-path recollisions, which are known to induce the smallest dipole chirp [6]. Above the 20th order, the harmonic peaks gradually increase their widths, suggesting that they are from the long-path recollisions, which induce larger dipole chirp. The same trend is recognizable for $\theta = \pi/3$ as well, although there is a narrow region of irregularity around the 30th order. The mechanism for this natural selection of a single-electron path in the o5 state is unclear, but it is not a multielectron effect in our model, as the signatures are found in the individual MO spectrum. In a separate calculation with a 1200 nm/1 $\times$ 10^{14} W cm^{-2} driving laser field, the spectra did not exhibit this behavior. Aside from this, the individual MO spectra for the 1200 nm/1 $\times$ 10^{14} W cm^{-2} driving laser field are found to have the same qualitative features as for the 800 nm/2 $\times$ 10^{14} W cm^{-2} field, and therefore are not shown in this paper.

The finding that many orbitals can contribute to multiphoton ionization and to HHG was demonstrated originally in a TDDFT model of ref. 15, using a semiempirical local exchange–correlation functional. In the more recent work using a time-dependent optimized effective potential [17], it was found that a considerable amount of orbital switching occurred as a function of molecular orientation angle, that is, that even the HOMO-2 in N_2 could dominate ionization from the molecule. A similar set of calculations, however, with a frozen molecular potential displayed the absence of such strong orbital switching effects in multiphoton ionization [42]. Given these substantial discrepancies of TDDFT calculations with and without dynamical screening effects, more model calculations are needed to understand the orbital response in molecule–laser interactions. It is desirable to extend our 2D model such that the role of the HOMO-2 in N_2 can be fully investigated, because in the present 2D model the HOMO-2 state (o2) is bound so deeply (cf. Table 1) that its contribution to HHG is negligible.

3.3.2. Net spectra

In this section, we examine the net dipole spectra $D(\omega)$ of the 2D N_2 and F_2 molecules, obtained either from $a^V(t)$ of (13), or from $a^W(t)$ of (14). Two sets of driving-laser frequency and peak-intensity settings are chosen in accordance with the experimental setups of ref. 30 (i.e., 800 nm/2 $\times$ 10^{14} W cm^{-2}, and 1200 nm/1 $\times$ 10^{14}W cm^{-2}).

Fig. 6. Net harmonic spectra (in arbitrary units) from the 2D N_2 molecule driven by (*a* and *c*) 800 nm/2 × 10^{14} W cm^{-2} and (*b* and *d*) 1200 nm/1 × 10^{14} W cm^{-2} laser fields, evaluated from (*a* and *b*) (13) as $|\tilde{a}^V(\omega)|^2$ and (*c* and *d*) (14) as $|\tilde{a}^W(\omega)|^2$: solid line, $\theta = 0$; dashed line, the angle-average; vertical lines indicate the positions of the semiclassical cutoffs for the HOMO.

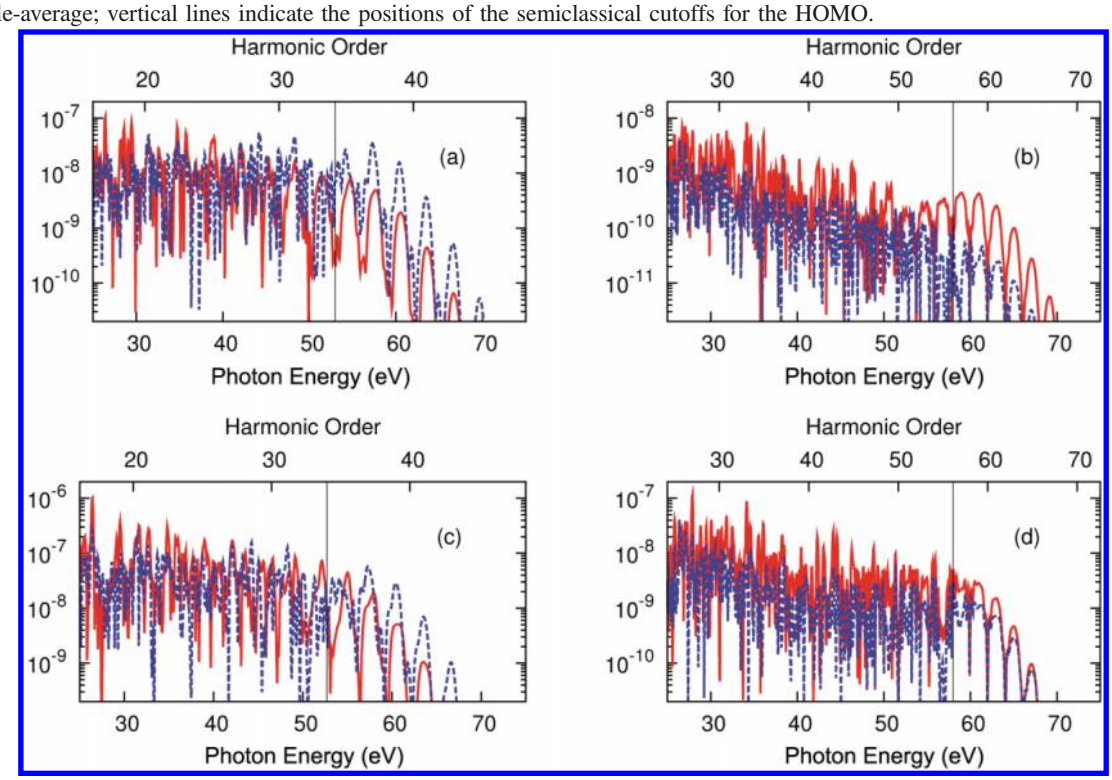

Figure 6 shows the square modulus of net dipole acceleration for N_2, for $\theta = 0$ (solid line) and for the angle-average (dashed line). They are shown vs. photon energy as well as vs. harmonic order, as in ref. 30. The results obtained from $a^V(t)$ using the two previously mentioned driving-laser settings are displayed in Figs. 6*a* and 6*b*, to be compared with the ones from $a^W(t)$ in Figs. 6*c* and 6*d* directly below. The angle-averaged spectra are based on seven calculations between $\theta = 0$ and $\pi/2$, $\Delta\theta = 15°$. The net dipole accelerations $\tilde{a}^V(\omega)$ or $\tilde{a}^W(\omega)$ for these different orientations are averaged coherently in frequency space to form the angle-averaged spectra.

Both a^V- and a^W-prescriptions predict the position of the harmonic cutoff between 50 and 60 eV, which is in agreement with the N_2 spectra of ref. 30. Here we define the cutoff in our single-molecule response spectra (without the propagation effect) as the location where the interference from degenerate electron paths gives way to well-resolved peaks at odd harmonic orders. Given the simplicity of our model, this agreement is encouraging and may justify an IPM description of molecular HHG.

The details of the spectra based on the two different prescriptions for the net dipole acceleration are rather different. For instance, the harmonic spectra based on $a^V(t)$ in Figs. 6*a* and 6*b* predict much smaller harmonic yield than the ones based on $a^W(t)$ in Figs. 6*c* and 6*d* for both the $\theta = 0$ and angle-averaged cases, which might mean that the inclusion of ∇v_{ee} in the $a^V(t)$ cancels the nuclear-potential contribution ∇U in the net harmonic spectrum. Because we are solving the TDSE with rather simplistic model potential (5) for v_{ee}, the calculation based on $a^V(t)$ is considered more consistent in our model than the one based on $a^W(t)$. One of the challenges of realistic TDDFT calculations for molecular HHG will be to demonstrate consistency in this regard, that is, to show that the net spectra calculated from both (13) and (14) do agree.

The experimental N_2 spectra in ref. 30, showed a local minimum around 40 eV regardless of the applied driving-laser intensities and frequencies, and therefore its origin was claimed to be not dynamical but structural. The fact that the observed minima in ref. 30, appeared at the same place for both the aligned ($\theta = 0$) and random-orientation cases could not be explained in terms of the the two-center interference effect [24]. In a follow-up paper by Jin et al. [49], it was shown that the 40 eV minimum in N_2 spectra is a property of the HOMO, similar to the Cooper minimum, which occurs in atomic HHG. The spectra of our 2D N_2 molecule in Fig. 6 fail to produce this minimum, as it must depend sensitively on the details of the molecular potential.

Figure 7 shows the net spectra for the 2D F_2 molecule: Figs. 7*a* and 7*b* are obtained from $a^V(t)$, while Figs. 7*c* and 7*d* from $a^W(t)$. Unlike for N_2, the spectra based on the two prescriptions are not very different for F_2, and the important spectral features are found in both cases. For instance, we find a broad minimum just below the HOMO cutoff in the $\theta = 0$ spectra of Figs. 7*a* and 7*c* driven by 800 nm/2 × 10^{14} W cm^{-2} laser fields, which resembles what is observed in ref. 30, for the CO_2 molecule, that is, the minimum does not occur in the angle-averaged spectrum but only when the molecule is aligned at $\theta = 0$. Because the first few valence MOs of CO_2 have similar symmetries as F_2, it is not surprising to see common features in their harmonics. The local

Fig. 7. Same as Fig. 6 but for the 2D F_2 molecule.

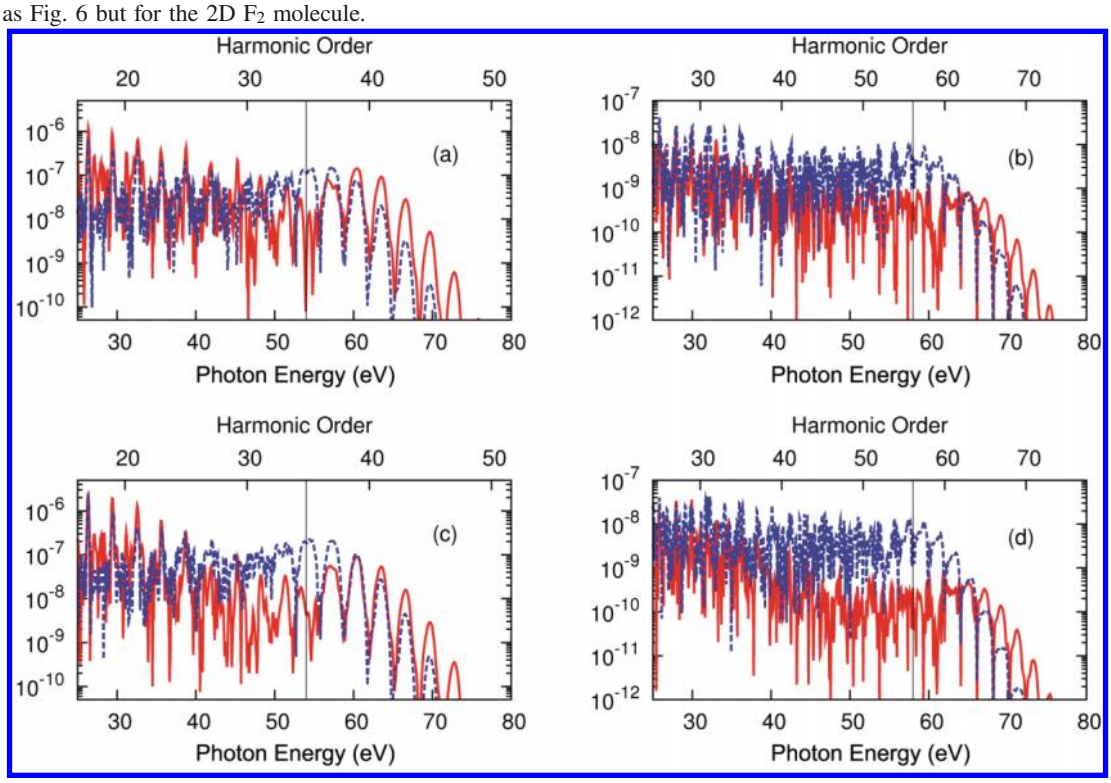

minimum in the CO_2 spectra of ref. 30, was found to shift its location depending on the driving-laser intensity, and therefore its cause was attributed to the orbital–orbital interference effect that depends on electron dynamics. In the following section, we will examine the phase differences between different MO contributions for our F_2 spectra to find some evidence for the orbital–orbital interference effects similar to the one in ref. 30. The spectra in Figs. 7*b* and 7*d* driven by 1200 nm/1 × 10^{14} W cm^{-2} laser fields do not exhibit a well-modulated minimum, but simply extend to the inner-MO cutoff for $\theta = 0$ where the HOMO-2 contribution dominates (Sect. 3.3.1).

3.4. Phase difference effects

It is known that the location of a dynamically-induced harmonic minimum in the CO_2 molecule is determined by the phase difference between the HOMO and HOMO-2 harmonic spectra [3]. For a given pair of MOs, labeled by n and n', one can write

$$D(\omega) \sim |\tilde{a}_n(\omega) + \tilde{a}_{n'}(\omega)|^2 = |\tilde{a}_n(\omega)|^2 + |\tilde{a}_{n'}(\omega)|^2 + |\tilde{a}_n(\omega)||\tilde{a}_{n'}(\omega)| \cos \Delta\phi_{nn'}(\omega) \quad (16)$$

where $\tilde{a}_n(\omega)$ and $\tilde{a}_{n'}(\omega)$ are the Fourier transforms of the dipole accelerations given by (12), and $\Delta\phi_{nn'}(\omega)$ is their phase difference. In situations where the two dipole accelerations are of similar magnitude, the interference term ($\sim\cos \Delta\phi_{nn'}$) determines the structure of the harmonic minimum [3, 30].

The individual MO spectra shown in Fig. 5 suggest that harmonics from the three outermost MOs of the 2D F_2 molecule, driven by an 800 nm/2 × 10^{14} W cm^{-2} laser field, all have comparable magnitudes in the plateau region when $\theta = 0$. We therefore expect to find the orbital–orbital interference effect in this case. In Fig. 8, we plot the phase difference for each pair of MO harmonics shown in Fig. 5 for $\theta = 0$. The harmonic phases are adjusted by adding some multiple of 2π

Fig. 8. Top panel: phase differences (in radians) among three different MO harmonics of the 2D F_2 molecule shown in Fig. 5 for $\theta = 0$: solid line, $\Delta\phi_{45}$; dashed line, $\Delta\phi_{34}$; and dash-dotted line, $\Delta\phi_{35}$. Horizontal lines are drawn at odd integer multiples of π to indicate destructive interference of an orbital pair. Middle panel: the solid line is the net harmonic spectrum of Fig. 7*a* at $\theta = 0$, i.e., the coherent sum of MO spectra in Fig. 5 given by (13). The dashed line shows an incoherent sum to highlight the predominant occurrence of destructive interferences. Bottom panel: same as the middle panel, but with the net spectrum of Fig. 7*c* given by (14).

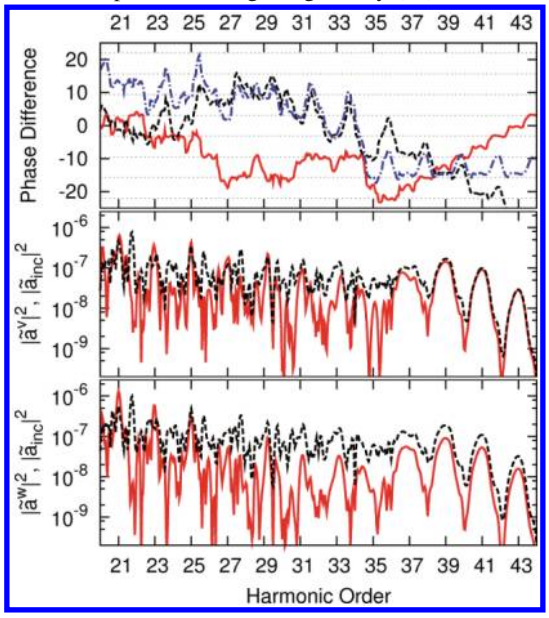

so that all three phase difference plots appear in the same frame between –25 and 25 radians. Horizontal lines are drawn at odd integer multiples of π where two orbital contributions can interfere destructively. Also shown in Fig. 8 are the corresponding net harmonic spectra evaluated from two different acceleration forms, that is, Figs. 7*a* and 7*c* for $\theta = 0$ (solid lines). The amount of orbital–orbital interference is represented by the difference between the coherent sum (solid line) found from (13) and (14) and the incoherent sum (dashed line) in the bottom two panels of Fig. 8, given by

$$|\widetilde{a}_{\mathrm{inc}}(\omega)|^2 = \sum_{n=1}^{N} |g_n \widetilde{a}_n(\omega)|^2 \tag{17}$$

In the top panel of Fig. 8, the phase differences $\Delta\phi_{34}$ (dashed line) and $\Delta\phi_{35}$ (dash-dotted line) exhibit similar profiles. On the other hand, the phase difference $\Delta\phi_{45}$ (solid line) follows a distinctive pattern; it tends to stabilize at odd integer multiples of π. The net spectra in the bottom two panels show clearer harmonic peaks than the incoherent sum in the plateau region, which is the effect of destructive interference due to $\Delta\phi_{45}$, as the locations where $\Delta\phi_{45}$ stabilizes often correspond to the suppressions in the net harmonics. Figure 5 shows that all three MOs have similar strengths in the plateau when $\theta = 0$. The o4 and o5 states of the 2D F_2 molecule, however, have occupation numbers of four, as compared to two for the o3 state. The net spectra in the plateau region must therefore be dominated by the o4 and o5 orbitals, as their amplitude is weighed more in the sum according to (13) or (14). This is why the phase difference $\Delta\phi_{45}$ controls the structure in the plateau in the net spectrum.

Beyond the 33rd harmonic, the o3 spectrum dominates over the outer two MO spectra in Fig. 5 for $\theta = 0$. As the intensities of the o4 and o5 harmonics fall off rapidly beyond their cutoffs, their contribution to the coherent sum is reduced, and their phase differences with respect to the o3 harmonics start to affect the net spectrum. The suppressions in the net harmonic spectra at the 33rd and 35th harmonic orders are indeed caused by $\Delta\phi_{34}$ and $\Delta\phi_{35}$, as their phase differences in Fig. 8 are at odd integer multiples of π at the 33rd and 35th orders, while $\Delta\phi_{45}$ (solid line) is not. Beyond the 37th order, the o3 spectra are two orders of magnitude stronger than the other two in Fig. 5 for $\theta = 0$, and therefore interference effects are not visible in the net spectra.

These main findings are independent of the acceleration forms; both a^{V}- and a^{W}-prescriptions predict destructive interference between harmonic orders 30 and 38. The net harmonic spectrum based on the a^{W}-prescription that is motivated by TDDFT produces more pronounced interference minima.

The phase differences in Fig. 8 are more complicated than the results of a SFA model presented in ref. 30, for two reasons. First, our TDSE calculation follows the complete evolution of the MO wavepacket, including strong-field dynamics, which leads to ionization, rescattering, and recombination in the three-step picture [45]. The calculation in ref. 30, is simpler, as it neglects the phase acquired during the ionization step. Secondly, our calculation does not distinguish different quantum paths of an ionized electron, whereas ref. 30, disregards the higher-order paths to be consistent with their experimental measurement, as the propagation effect selects only the short-path solution. The phases observed for the individual-MO spectrum $|\widetilde{a}_n(\omega)|^2$ in the present model calculation are similar to those found in full-dimensional TDSE calculations for atomic HHG [47], and thus they are deemed to be accurate representations in 2D.

4. Conclusion

In this paper, HHG spectra from closed-shell diatomic molecules in 2D are calculated by solving the single-electron TDSE for a few outermost occupied MOs. The net harmonic spectra from multiple orbitals are evaluated in two ways, either as a coherent sum of individual MO spectra, or from the net dipole acceleration according to TDDFT. Our IPM calculations predict that the high harmonic spectra from individual MOs obey the semiclassical cutoff law. However, the relative strengths among these MOs vary depending on molecular orientations, as the overall harmonic yield decreases when the molecule is oriented at an angle that suppresses the ionization. Such ionization-suppressing angles cannot be determined for all linear molecules simply based on the binding character of their MOs, as they may also depend on the internuclear separation and other structural factors.

Concerning the net spectrum, the contributions from different MOs become comparably strong when a molecule is oriented in such a way that the spectral strength of the HOMO harmonic weakens due to the ionization suppression. This causes the net spectrum to extend to the inner MO cutoffs, and in some cases creates a local minimum due to destructive interferences. Our finding is consistent with the explanations given for the intensity-dependent minimum of CO_2 spectra based on the SFA approach [3, 30].

The 2D IPM calculation presented in this work cannot provide a complete explanation of experimental spectra. A recent experiment–theory collaboration has accomplished that by dealing with both the single-molecule response in the strong laser field and the harmonic propagation in the ionizing medium [50]. Nevertheless, our work demonstrates how far a reduced-dimensional TDSE calculation can account for structural and multielectron effects beyond the single-active-electron approximation. The present model should serve as a useful testing ground for relevant ideas concerning multielectron dynamics in molecular HHG.

Acknowledgments

This work has been supported by the Natural Science and Engineering Research Council, Canada, and by SHARCNET.

References

1. M. Lein, N. Hay, R. Velotta, J.P. Marangos, and P.L. Knight. Phys. Rev. Lett. **88**, 183903 (2002). doi:10.1103/PhysRevLett.88.183903. PMID:12005685.
2. B.K. McFarland, J.P. Farrell, P.H. Bucksbaum, and M. Gühr. Science, **322**, 1232 (2008). doi:10.1126/science.1162780. PMID:18974318.
3. O. Smirnova, Y. Mairesse, S. Patchkovskii, N. Dudovich, D. Villeneuve, P. Corkum, and M.Y. Ivanov. Nature, **460**, 972 (2009). doi:10.1038/nature08253.
4. J.L. Krause, K.J. Schafer, and K.C. Kulander. Phys. Rev. Lett.

68, 3535 (1992). doi:10.1103/PhysRevLett.68.3535. PMID: 10045729.
5. J.L. Krause, K.J. Schafer, and K.C. Kulander. Phys. Rev. A, **45**, 4998 (1992). doi:10.1103/PhysRevA.45.4998. PMID: 9907584.
6. M. Lewenstein, P. Balcou, M.Y. Ivanov, A. L'Huillier, and P.B. Corkum. Phys. Rev. A, **49**, 2117 (1994). doi:10.1103/PhysRevA.49.2117. PMID:9910464.
7. M. Lewenstein, P. Saliéres, and A. L'Huillier. Phys. Rev. A, **52**, 4747 (1995). doi:10.1103/PhysRevA.52.4747. PMID: 9912816.
8. A.-T. Le, R.R. Lucchese, S. Tonzani, T. Morishita, and C.D. Lin. Phys. Rev. A, **80**, 013401 (2009). doi:10.1103/PhysRevA.80.013401.
9. R. Santra and A. Gordon. Phys. Rev. Lett. **96**, 073906 (2006). doi:10.1103/PhysRevLett.96.073906. PMID:16606094.
10. M.Y. Ivanov, T. Brabec, and N. Burnett. Phys. Rev. A, **54**, 742 (1996). doi:10.1103/PhysRevA.54.742. PMID:9913532.
11. O. Smirnova, S. Patchkovskii, Y. Mairesse, N. Dudovich, D. Villeneuve, P. Corkum, and M.Y. Ivanov. Phys. Rev. Lett. **102**, 063601 (2009). doi:10.1103/PhysRevLett.102.063601. PMID: 19257587.
12. G.L. Kamta and A.D. Bandrauk. Phys. Rev. A, **71**, 053407 (2005). doi:10.1103/PhysRevA.71.053407.
13. N. Nguyen and A.D. Bandrauk. Phys. Rev. A, **73**, 032708 (2006). doi:10.1103/PhysRevA.73.032708.
14. X. Chu and P.J. Memoli. Chem. Phys. **391**, 83 (2011). doi:10.1016/j.chemphys.2011.03.024.
15. X. Chu and S.-I. Chu. Phys. Rev. A, **64**, 063404 (2001). doi:10.1103/PhysRevA.64.063404.
16. J. Heslar, J. Carrera, D. Telnov, and S.-I. Chu. Int. J. Quantum Chem. **107**, 3159 (2007). doi:10.1002/qua.21491.
17. D.A. Telnov and S.-I. Chu. Phys. Rev. A, **80**, 043412 (2009). doi:10.1103/PhysRevA.80.043412.
18. S.-K. Son and S.-I. Chu. Phys. Rev. A, **80**, 011403 (2009). doi:10.1103/PhysRevA.80.011403.
19. E.P. Fowe and A.D. Bandrauk. Phys. Rev. A, **81**, 023411 (2010). doi:10.1103/PhysRevA.81.023411.
20. M. Abu-samha and L.B. Madsen. Phys. Rev. A, **81**, 033416 (2010). doi:10.1103/PhysRevA.81.033416.
21. Q. Su and J.H. Eberly. Phys. Rev. A, **44**, 5997 (1991). doi:10.1103/PhysRevA.44.5997. PMID:9906662.
22. M. Protopapas, D. Lappas, and P. Knight. Phys. Rev. Lett. **79**, 4550 (1997). doi:10.1103/PhysRevLett.79.4550.
23. E. van der Zwan and M. Lein. Phys. Rev. A, **82**, 033405 (2010). doi:10.1103/PhysRevA.82.033405.
24. M. Lein, N. Hay, R. Velotta, J.P. Marangos, and P.L. Knight. Phys. Rev. A, **66**, 023805 (2002). doi:10.1103/PhysRevA.66.023805.
25. T. Kreibich, M. Lein, V. Engel, and E. Gross. Phys. Rev. Lett. **87**, 103901 (2001). doi:10.1103/PhysRevLett.87.103901. PMID:11531478.
26. S. Pieper and M. Lein. Phys. Rev. A, **77**, 041403 (2008). doi:10.1103/PhysRevA.77.041403.
27. M. Lein, T. Kreibich, E.K.U. Gross, and V. Engel. Phys. Rev. A, **65**, 033403 (2002). doi:10.1103/PhysRevA.65.033403.
28. A.D. Bandrauk and H. Lu. Phys. Rev. A, **72**, 023408 (2005). doi:10.1103/PhysRevA.72.023408.
29. S. Sukiasyan, C. McDonald, C. Destefani, M.Y. Ivanov, and T. Brabec. Phys. Rev. Lett. **102**, 223002 (2009). doi:10.1103/PhysRevLett.102.223002. PMID:19658861.
30. H.J. Wörner, J.B. Bertrand, P. Hockett, P.B. Corkum, and D.M. Villeneuve. Phys. Rev. Lett. **104**, 233904 (2010). doi:10.1103/PhysRevLett.104.233904. PMID:20867243.
31. M.B. Gaarde, J.L. Tate, and K.J. Schafer. J. Phys. At. Mol. Opt. Phys. **41**, 132001 (2008). doi:10.1088/0953-4075/41/13/132001.
32. K.C. Kulander. Phys. Rev. A, **36**, 2726 (1987). doi:10.1103/PhysRevA.36.2726. PMID:9899177.
33. K.J. Schafer. *In* Strong Field Laser Physics. *Edited by* T. Brabec. Springer Science+Business Media, LLC. 2008. Chap. 6, pp. 111–145.
34. G. Vignale. Phys. Rev. Lett. **74**, 3233 (1995). doi:10.1103/PhysRevLett.74.3233. PMID:10058145.
35. M.A. Marques, C.A. Ullrich, F. Nogueira, A. Rubio, K. Burke, and E.K.U. Gross (*Editors*). Time-dependent Density Functional Theory, Lecture notes in physics, Vol. 706. Springer, Berlin. 2006.
36. A. Gordon, F.X. Kärtner, N. Rohringer, and R. Santra. Phys. Rev. Lett. **96**, 223902 (2006). doi:10.1103/PhysRevLett.96.223902. PMID:16803307.
37. C.W. Scherr. J. Chem. Phys. **23**, 569 (1955). doi:10.1063/1.1742031.
38. A.C. Wahl. J. Chem. Phys. **41**, 2600 (1964). doi:10.1063/1.1726327.
39. A. Lofthus and P.H. Krupenie. J. Chem. Phys. Ref. Data, **6**, 113 (1977). doi:10.1063/1.555546.
40. X. Chu and S.-I. Chu. Phys. Rev. A, **70**, 061402 (2004). doi:10.1103/PhysRevA.70.061402.
41. D. Dundas and J.M. Rost. Phys. Rev. A, **71**, 013421 (2005). doi:10.1103/PhysRevA.71.013421.
42. V.I. Usachenko, P.E. Pyak, and V.V. Kim. Phys. Rev. A, **79**, 023415 (2009). doi:10.1103/PhysRevA.79.023415.
43. A.B. Cornford, D.C. Frost, C.A. McDowell, J.L. Ragle, and I.A. Stenhouse. J. Chem. Phys. **54**, 2651 (1971). doi:10.1063/1.1675227.
44. J. Muth-Böhm, A. Becker, and F.H.M. Faisal. Phys. Rev. Lett. **85**, 2280 (2000). doi:10.1103/PhysRevLett.85.2280. PMID: 10977991.
45. P.B. Corkum. Phys. Rev. Lett. **71**, 1994 (1993). doi:10.1103/PhysRevLett.71.1994. PMID:10054556.
46. B. Shan, X.-M. Tong, Z. Zhao, Z. Chang, and C.D. Lin. Phys. Rev. A, **66**, 061401 (2002). doi:10.1103/PhysRevA.66.061401.
47. K.J. Schafer and K.C. Kulander. Phys. Rev. Lett. **78**, 638 (1997). doi:10.1103/PhysRevLett.78.638.
48. P. Antoine, A. L'Huillier, and M. Lewenstein. Phys. Rev. Lett. **77**, 1234 (1996). doi:10.1103/PhysRevLett.77.1234. PMID: 10063025.
49. C. Jin, J.B. Bertrand, R.R. Lucchese, H.J. Wörner, P.B. Corkum, D.M. Villeneuve, A.-T. Le, and C.D. Lin. Phys. Rev. A, **85**, 013405 (2012). doi:10.1103/PhysRevA.85.013405.
50. C. Jin, H.J. Wörner, V. Tosa, A.-T. Le, J.B. Bertrand, R.R. Lucchese, P.B. Corkum, D.M. Villeneuve, and C.D. Lin. J. Phys. At. Mol. Opt. Phys. **44**, 095601 (2011). doi:10.1088/0953-4075/44/9/095601.